UWB Processing Applied to Multifrequency Radar Sounders: The Case of MARSIS and Comparison With SHARAD

L. Gambacorta, M. C. Raguso, M. Mastrogiuseppe, and R. Seu

Abstract— We readapt ultrawideband (UWB) processing to enhance the range resolution of the Mars Advanced Radar for Subsurface and Ionosphere Sounding (MARSIS) up to a factor of 6 (25 m). The technique provides for the estimation of radar signature over a wider spectrum via the application of well-known super-resolution (SR) techniques to adjoining subbands. The measured spectra are first interpolated and then extrapolated outside the original bands. The revised algorithm includes the estimation and removal of ionospheric effects impacting the two signals. Because the processing requires the realignment of the echoes at different frequencies, we derived the maximum tolerable retracking error to obtain reliable super-resolved range profiles. This condition is fulfilled by low-roughness areas compared to MARSIS wavelength, which proves to be suitable for the application of our processing. Examples of super-resolved experimental products over different geological scenarios show the detection of shallow dielectric interfaces not visible from original MARSIS products. Our results are validated by comparison with the Shallow Radar (SHARAD) data acquired at the crossovers, demonstrating the potential of the method to provide enhanced imaging capabilities.

Index Terms— Autoregressive (AR) models, bandwidth extrapolation (BWE), bandwidth interpolation (BWI), ground penetrating radar (GPR), ionosphere effects, radar sounder, surface roughness.

I. INTRODUCTION

GROUND penetrating radars (GPRs) from orbit, also called sounders, have gained popularity in recent years as geophysical imaging tools oriented to acquire information about the crustal composition, subsurface topography, and morphology of planets and moons. The Mars Advanced Radar for Subsurface and Ionosphere Sounding (MARSIS) [1] and the Shallow Radar (SHARAD) [2], currently employed in

Mars exploration, are today the only instruments aimed to perform remote geological investigations in the upper portions of Martian crust down to a few kilometers' depth [3].

Sounders usually adopt wideband electromagnetic (EM) signals operating in the high-frequency (HF) or very HF (VHF) band. For subsurface sounding (SS) exploration, the design of the operative frequency represents a tradeoff between penetration depth, resolution capabilities, and ionospheric condition, which distorts and attenuates signals close or below the plasma frequency [4]. In standard sounder imaging processing, the range resolution is limited by Rayleigh' criterion, which poses as technological limit the transmitted radar bandwidth.

Efforts to improve imaging capabilities of radar data have been done during the 1990s by the Radar Imaging Techniques Group at Lincoln Laboratory. They developed a robust signal processing technique called bandwidth extrapolation (BWE) demonstrating the potentials of autoregressive (AR) models in enhancing range resolution and supporting scientific analysis of radar imagery from satellites and aircraft [5]. In 1997, the same concepts were proposed by Thomas G. Moore in order to fill the missing samples in the range-compressed spectrum of multiband radars. The method, also known as bandwidth interpolation (BWI) technique, involved the extrapolation of the two subbands followed by a weighted sum of the samples to reconstruct the missing portion between the available spectra [6]. Few years later, the same method was revisited by Cuomo et al. [7], where they addressed the possibility to overcome resolution limitations by proposing an ultrawideband (UWB) coherent processing to extrapolate radar signature of a target by using sparse subbands and accurately estimate targets range profiles with higher resolution. Originally designed for radar tracking systems, these techniques have been recently tested and validated on experimental data acquired by planetary radars, such as SHARAD [8], MARSIS [9], the Cassini Radar [10], [11], and a prototype of the GPR WISDOM onboard of the future ExoMars mission [12]. A single BWE has been successfully exploited to both enhance data range resolution and suppress EM interferences (EMIs) [8], [9].

Here, we exploit the potentiality of MARSIS quasi-simultaneous data acquisition design by applying UWB techniques to the signals received at two different channels. After compensating for the ionospheric effects (e.g., time delay, phase shift, and attenuation), we fill the missing sample between the subbands via BWI with a result of a full 2-MHz

band and then use BWE to synthesize the final 6-MHz bandwidth.

With the aim of applying UWB to experimental MARSIS data, we derive a condition for the applicability of the technique that is suitable over smooth regions where time-delay compensation can be properly performed using retracking algorithms. We investigate time-delay errors through ray-traced Mars Orbiter Laser Altimeter (MOLA) simulated radargrams and evaluate the distortion effects given by residual misalignment of echoes.

This article is organized as follows. In Section II, we provide the main design features of the MARSIS dataset used for the application of our processing. In Sections III, we describe in detail the BWE/BWI techniques based on AR models. In Section IV, we focus on the redesigned UWB processing for the MARSIS data and discuss the retrieval of the correction parameters to compensate for the ionosphere effects on the signals.

In Section V, we validate the expected resolution improvement and analyze the effects of time-delay residual errors to constrain the areas suitable for the algorithm. Finally, Section VI presents the results of the UWB MARSIS data processing and the comparison with SHARAD data.

II. SOUNDERS DATASET DESCRIPTION

A. MARSIS Dataset

MARSIS, onboard the European Space Agency's Mars Express orbiter (MEX), has been probing Mars surface since 2005, successfully acquiring SS data on more than 20 000 orbits. The radar consists of a digital subsystem, transmitter, receiver modules, and two antennas: a 40-m dipole for transmit and receive and a 7-m receive-only monopole element originally designed for clutter cancellation [1].

In its SS modes, MARSIS typically operates with two of the four-frequency 1-MHz channels (B1, B2, B3, and B4 centered at 1.8, 3, 4, and 5 MHz, respectively), using instantaneous linear frequency-modulated waveforms ("chirp") that provide a 150-m free-space vertical range resolution. The along-track resolution is approximately 5–9 km obtained using unfocused synthetic aperture processing implemented onboard, while the cross-track spatial resolution is about 10–40 km depending on the roughness condition of the surface. Off-nadir clutter can be modeled using MOLA topographic data [13], and the comparison with MARSIS radargrams provides a robust method to identify clutter echoes [14], [15].

We use SS3 data to apply our UWB processing because of the quasi-simultaneous acquisition of the same area using a two-frequency single-antenna mode and as providing complex data format on the three Doppler filters. The operational bands are selected based on the expected local ionospheric condition that could cause the surface (and subsurface) detection to be compromised. During nighttime, the lowest frequencies are usually adopted, while for the dayside, the highest is preferred [16]. Azimuth processing is performed onboard to reduce the amount of data to be downloaded, while range compression is performed on ground. Furthermore, unfocused synthetic aperture radar (SAR) processing involves the coherent sum of a different number of pulses in the synthetic aperture to guarantee continuity in the surface observation and the same along-track resolution between the acquired products [4].

B. SHARAD Dataset

SHARAD, onboard the NASA orbiter Mars Reconnaissance Orbiter (MRO), has been probing around Mars since 2008. It is composed of two main physical elements, the SHARAD electronics box (SEB) and a 10-m dipole antenna.

The sounder transmits signals at the 20-MHz center frequency with a 10-MHz bandwidth. The synthetic aperture processing yields an along-track resolution between 0.3 and 1 km and a cross-track resolution between 3 and 6 km, due to the pulse-limited design [17]. The SHARAD wavelength is greater than the ionosphere plasma frequency, allowing it to propagate through with less distortions respect to MARSIS. However, phase dispersion is corrected on the ground by the phase gradient autofocus (PGA) method.

SHARAD's operative frequency and wideband features result in a significantly better resolution when compared to MARSIS (15 versus 150 m), but with a reduction of penetration capabilities.

III. BWE AND BWI TECHNIQUES

The application of super-resolution (SR) on single-bandwidth MARSIS products has already demonstrated the possibility to obtain a resolution threefold improvement at the single channel [8]. Here, we propose to further enhance MARSIS range resolution (compared to the previous studies) by processing the data by means of the UWB method. The technique exploits both the subbands acquired by the radar that are merged by sample interpolation and then extrapolated by means of SR.

All these methods are based on spectral estimation theory and make use of AR and autoregressive moving average (ARMA) models, suitable for the application to radar data [5], [18], [19]. In fact, the pulse-compressed radar response from targets can be modeled in the frequency domain as a sum of complex sinusoids, with each frequency determined by the range delay of each scatter in the time domain [20]. The use of this a priori information allows to use parametric methods to pursue the spectral estimation of the sinusoids composing the signal, enabling to achieve higher resolution compared to a nonparametric model [21]. Based on this estimation, it is possible to predict the signal outside the acquisition bandwidth and after IFFT to obtain the super-resolved product in the delay space [1].

The method we have selected for our work is the AR model, both for BWE and BWI, which provides the solution of a linear system to estimate the prediction coefficients. This approach has been already successfully applied to sounder radar data, guaranteeing a reliable solution without incurring in unstable solution of the all-pole system [5], [18].

A. AR Linear Prediction

The AR model assumes that the sum of an evenly spaced set of signal samples x_{n-i}, multiplied by a set of complex

weights, or prediction coefficients a_i, will predict the next sample x_n. This set of constant weights can be moved ahead to continue the predictions and extrapolate the original data in a forward direction. The linear-prediction coefficients can be estimated in the frequency domain via mean-squared error (mse) minimization between the predicted signal and the actual measured data.

The forward prediction error can be described as follows:

$$E_n^f = x_n - \hat{x}_n^f \tag{1}$$

for $n = p + 1, \ldots, N$, where x_n is the nth frequency sample and $\hat{x}_n^f$ is its estimate using the AR forward prediction model

$$\hat{x}_n^f = -\sum_{i=1}^{p} a_i x_{n-i}. \tag{2}$$

In the same way, the backward prediction error

$$E_n^b = x_n - \hat{x}_n^b \tag{3}$$

for $n = 1, \ldots, N - p$, where $\hat{x}_n^b$ is the estimate of the nth spectrum sample x_n using the AR backward prediction model, is defined as follows:

$$\hat{x}_n^b = -\sum_{i=1}^{p} a_i^* x_{n+i} \tag{4}$$

where p is the order of the prediction filter, a_i is the ith predictor coefficient, a_i^* is its complex conjugate, and N is the total number of frequency data samples.

The total prediction error power to be minimized for a set of a_i can be defined as

$$E = \frac{1}{2} \sum_n \left| E_n^f \right|^2 + \left| E_n^b \right|^2. \tag{5}$$

The problems result in finding the solution of the Yule–Walker linear system, which provides the estimation of the prediction coefficients. Several methods have been developed to sort it out while reducing its computational cost, such as the covariance method, the Burg method, and the maximum likelihood estimator (MLE) [21].

B. Bandwidth Extrapolation

The radar response of a target in the frequency domain can be defined as

$$V(f) = \sum_i A_i(f) e^{\frac{j4\pi f R_i}{c}} \tag{6}$$

where f is the radar frequency and c is the speed of light in vacuum. The summation is over the number of targets associated with multiple reflections. Each scattering center is characterized by its amplitude A_i and its effective range R_i.

A frequency response expressed by (6) can be approximated by a linear-prediction AR model with a uniformly sampled frequency spectrum, which is given by

$$v[n] = V(n\delta f) \tag{7}$$

where δf is the frequency step between data samples. $v[n]$ are used to estimate the prediction coefficients that describe the sinusoid behavior outside the existent radar bandwidth,

thus enabling to forward and backward extend it. A linear-prediction model of the signal is combined with the measured radar data to synthesize extrapolated data outside the measured bandwidth as follows:

$$v_e[n] = \begin{cases} -\sum_{i=1}^{p} a[i]v[n - i] & \text{forward} \\ -\sum_{i=1}^{p} a^*[i]v[n + i] & \text{backward} \end{cases} \tag{8}$$

where $a[i]$ are the model coefficients and p is the model order employed for the extrapolation.

We choose the Burg method to pursue this estimation as most robust at different extrapolation factors, providing the lower extrapolation error compared to the other tested methods [22]. The algorithm has demonstrated to be well suited for the sounder signal, computationally efficient, and yielding to a stable linear-prediction filter due to the presence of a constraint in the parameter estimation. Such constraint, called the Levinson recursion, allows the unknown coefficient to be estimated iteratively at each step due to a sequence of least-square minimizations [21].

Extrapolation is generally performed over a portion of the spectra where samples at the edges (about 5% on each side) are removed to reduce spectral distortions [5].

The extrapolated spectrum yields a range resolution enhancement up to a factor of 3.

C. Bandwidth Interpolation

BWE for single channel can be used as an interpolator for reconstructing vacant band samples between two sparse subbands. This technique, called BWI, aims to fill this gap via a weighted sum of the forward and backward extrapolated subbands [6].

Considering data missing from $n = B$ to $n = E$ (see Fig.1), respectively, for low-frequency and HF bands, the data can be defined as follows:

$$v_3[n] = \begin{cases} v[n], & \text{for } 1 \ll n < B \\ 0, & \text{elsewhere} \end{cases} \tag{9}$$

$$v_4[n] = \begin{cases} v[n], & \text{for } E < n \ll N \\ 0, & \text{elsewhere.} \end{cases} \tag{10}$$

The AR methods used for BWE can also be applied to BWI problems: the HF and low frequency are, respectively, backward and forward extrapolated to completely fill the gap as

$$v_3[n] = -\sum_{i=1}^{P_3} a_3[i]v_3[n - i] \tag{11}$$

$$v_4[n] = -\sum_{i=1}^{P_4} a_4^*[i]v_4[n + i] \tag{12}$$

where the $a_3[i]$ and $a_4^*[i]$ coefficients are the Burg coefficients and the constants p_3 and p_4 are Burg model orders for HF and low-frequency data, respectively. Finally, the vacant band samples are obtained through a weighted sum of the
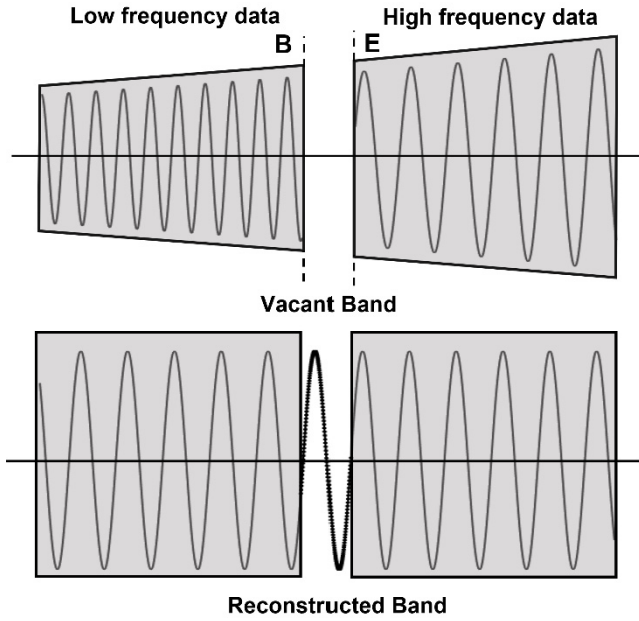
Fig. 1.   (Top) Representation in the Fourier domain of data acquired at two adjoining channels with a gap in between. The two subbands show the different effects caused by the propagation through a dispersive medium such as the ionosphere: constant and linear phase shift (the latter corresponding to a differential delay between the compressed signal in time domain). (Bottom) After ionosphere compensation consisting in estimation via LSE procedure, retracking and theoretical modeling, the UWB processing can be applied over the spectra. The two spectra are interpolated in order to predict the spectrum samples in the vacant band (BWI), and the samples predicted from the two spectra and their weighted mean are used to completely fill the gap.
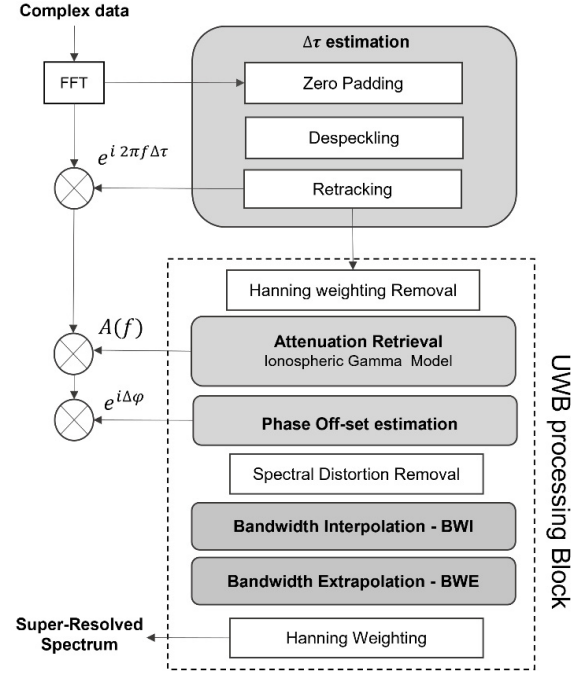

Fig. 2.   Schematic of the UWB processing flow. The complex signal is transformed into the frequency domain first, via FFT, and zero-padded. It is transformed back in the time domain for despeckling and $\Delta\tau$ estimation. The second block represents the core of the UWB processing. It consists of attenuation and phase offset estimation and compensation, and then, BWI and BWE procedures are applied to merge the bands and predict the samples outside the measured band. These operations are pursued after the removal of weighting functions (Hanning window in the case of MARSIS) and signal calibration. Finally, the final UWB processed product is obtained via IFFT.
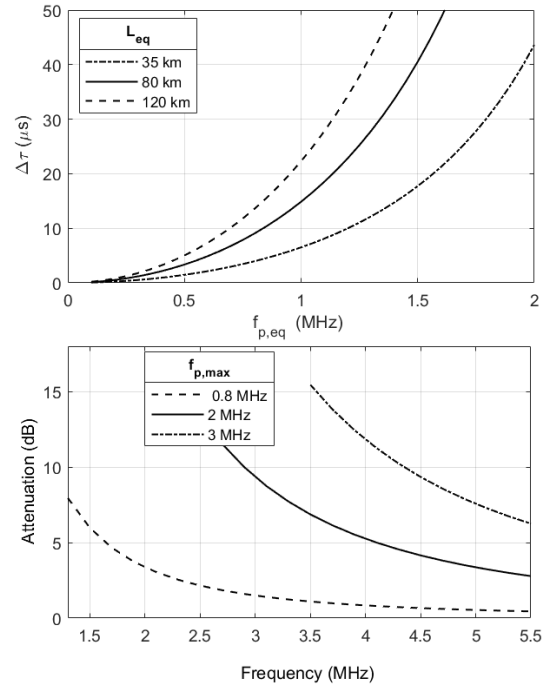
extrapolated data where the weights depend on the distance from the extrapolation band

$$\hat{v}[n] = \left(\frac{E-n}{E-B} \right) v_3[n] + \left(\frac{n-B}{E-B} \right) v_4[n] \qquad (13)$$

where $\hat{v}[n]$ are reconstructed data and $B \leq n \leq E$.

IV. UWB PROCESSING AND IONOSPHERE COMPENSATION

Here, we redesign the UWB method proposed by Cuomo et al. [7] to make it suitable for MARSIS data. Since the radar operates in the presence of the ionosphere, the processing requires an additional step consisting in the estimation and the correction of its dispersive effects on the received signals. Any residual will cause the distortion of the main lobe and spurious echoes after UWB. Time delay is corrected in the delay space via a retracking procedure, while phase offset and attenuation are in the frequency domain, exploiting BWE and ionospheric theoretical models, respectively. After this compensation, the spectra can be properly merged via interpolation procedure to fill the vacancy due to spectral distortion removal. Note that both parameter optimization and the average of predicted samples in the interpolation procedure cause the UWB method to act as a nonlinear filter on the input data.

The proposed technique yields a maximum attainable range resolution improvement up to a factor of 6 (25 m in free space) with respect to the single channel (150 m) if two

Fig. 3.   (Top) Ionospheric time delay as a function of equivalent plasma frequency. The curve is obtained for different values of L_{eq} as a numerical solution of (15) considering the bands B2 (3 MHz) and B3 (4 MHz). (Bottom) Ionospheric attenuation functions (dB) for expected maximum plasma frequencies in the case of Mars.

adjoining subbands are considered (e.g., B2 and B3). In the case of acquisitions over sparse bands (such as B2 and B4),
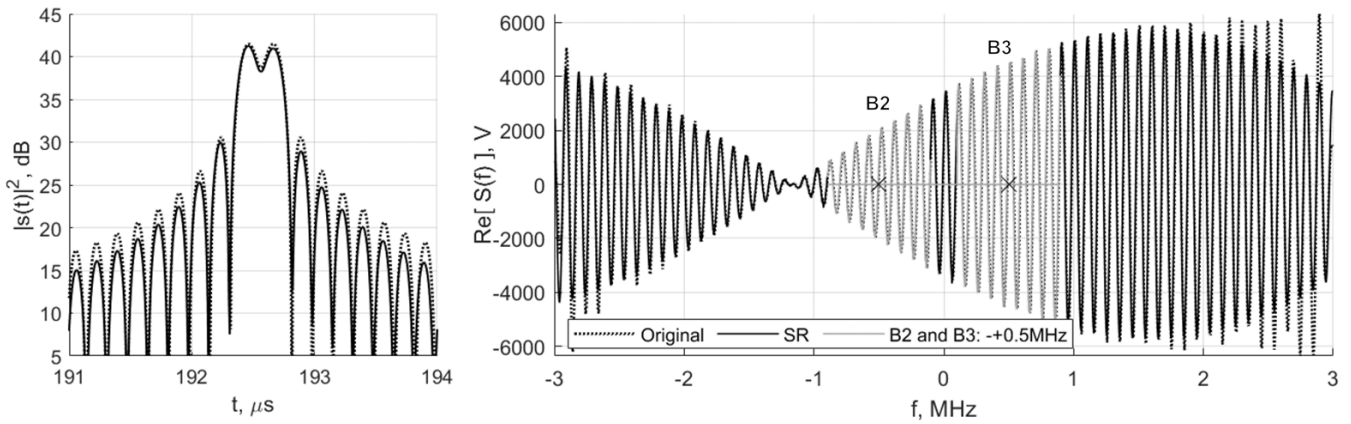
Fig. 4. Results from the 6-MHz band simulator, the UWB technique is applied to simulated response of two-point scatterers placed at the resolution limit (25 m). The method is applied to the two subbands B2 and B3 (gray line), extracted from the simulated spectrum (black dotted line). The subbands are interpolated, and the resulting 2-MHz spectrum extrapolated. Then, the super-resolved (black line) echoes (left) and the real part of the spectra (right) are compared to the 6-MHz original simulated signal, showing that the two echoes in the simulated response can now be detected even in the UWB processed product. The simulation parameters (such as bandwidth and sampling frequency) are the ones of MARSIS, but the study and results have general applicability.
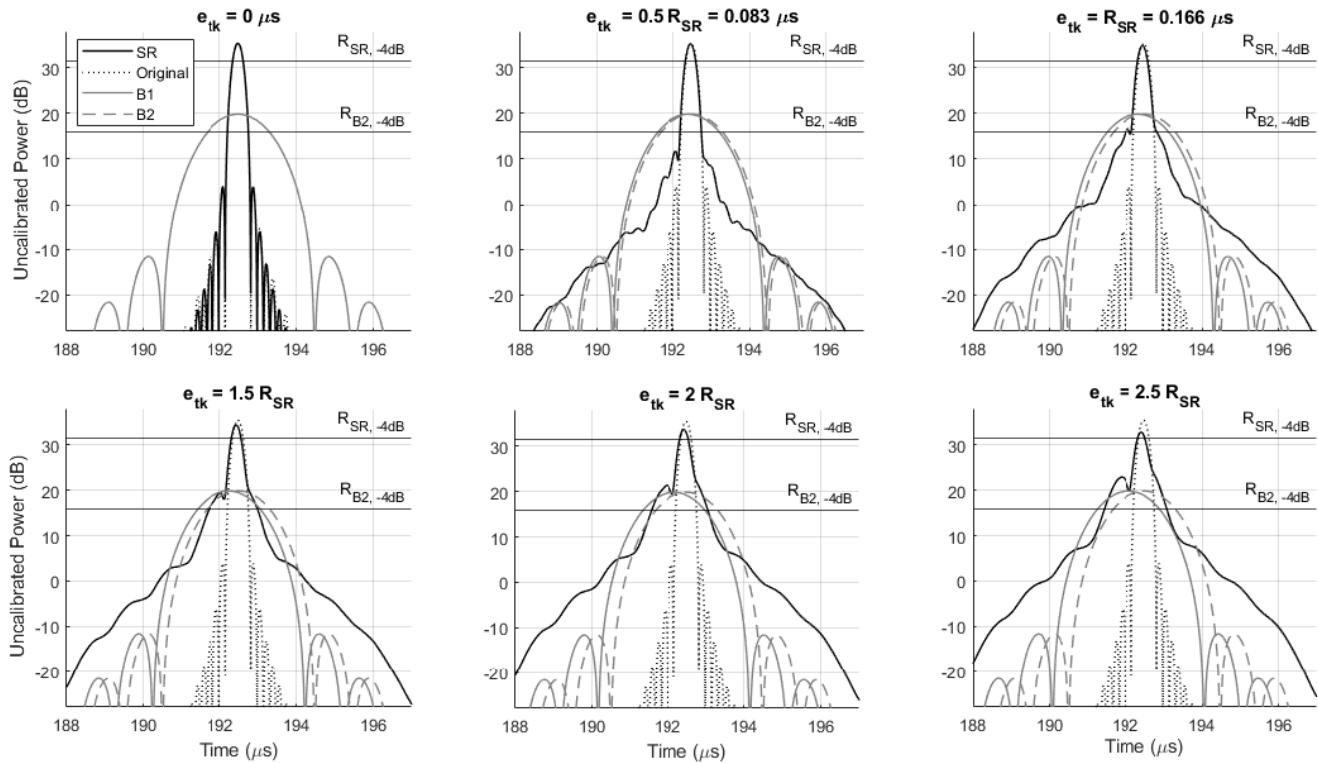

Fig. 5. Results from the UWB processing for different values in $\Delta\tau$ error (taken as multiples of the SR resolution). The method is applied to a simulated 6-MHz single-point scatter, as explained in Fig. 4. Here, the gray lines refer to signals from the two subbands, while the black solid line and the dotted line refer to the original and the UWB processed product, respectively. The resulting reflectors overlap in the case of no tracking errors while assuming strong differences when the error increases (spurious echoes). Therefore, a limit on the maximum tolerable error is set for the application of the algorithm corresponding to the SR resolution.

the potentialities of the algorithm could be extended, and after the interpolation of a 1.1-MHz vacancy, followed by BWE, the range resolution enhancement could be further improved.

The whole process can be summarized by the following steps (see Fig. 2):

1) ionospheric parameters estimation and spectra calibration;

2) spectra fusion via BWI;

3) spectrum prediction via BWE.

A. Ionospheric Time-Delay Estimation

Time delay introduced by the ionosphere can be modeled through the single parameter equivalent model (SPEM) [23], where it is assumed as a medium with constant plasma
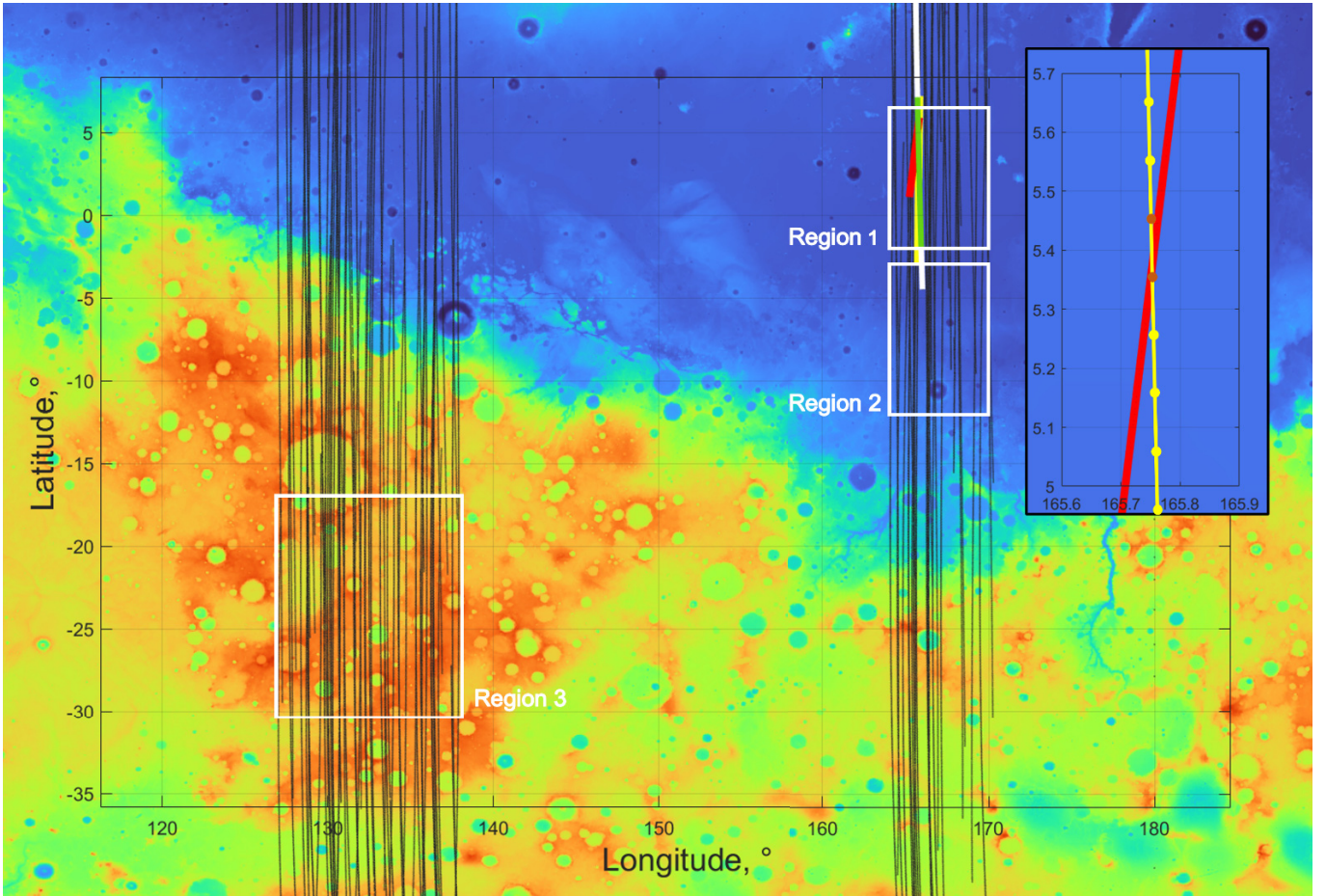
Fig. 6. MGS/MOLA surface elevation map depicting areas under analysis at three different roughness regimes (1: low, 2: medium, and 3: high). The black tracks are used for the $\Delta\tau$ statistical analysis on simulated data by selecting only the frames within the white square. Instead, the white track corresponds to the ray-traced simulation of the product ID 11264 MEX ray-traced MOLA simulation (see Fig. 8). The frames highlighted in green correspond to the UWB processed frames presented in Fig 9. The black box on the right shows a zoom over the area of interest where the yellow and the red tracks refer to the experimental observations from MARSIS (ID 16319) and SHARAD (ID 0771701) orbits, respectively. Orange dots at the crossover are used to underline the UWB processed MARSIS and SHARAD frames shown in Fig. 10.

frequency $f_{p,\text{eq}}$ along its vertical profile and with a fixed length L_{EQ}. Under this hypothesis, the phase distortion model describes ionosphere dispersive effects on the received signal as follows:

$$\Delta\varphi = \frac{4\pi L_{\text{EQ}}}{c} f \left(\sqrt{1 - \left(\frac{f_{p,\text{eq}}}{f}\right)^2} - 1 \right)$$

$$\cong a_0 + a_1(f - f_0) + a_2(f - f_0)^2 + a_3(f - f_0)^3$$
$$+ a_4(f - f_0)^4 + \cdots \qquad (14)$$

MARSIS L2 processing provides for the compensation of the terms from the second order onward but not of the constant and linear phase shifts, the latter causing a frequency-dependent delay of the echo

$$\Delta\tau = \tau_{fA} - \tau_{fB} = \frac{\tau_0}{\sqrt{1 - \frac{f_{p,\text{eq}}^2}{f_A^2}}} - \frac{\tau_0}{\sqrt{1 - \frac{f_{p,\text{eq}}^2}{f_B^2}}} \qquad (15)$$

where f_A and f_B are the two carriers and $\tau_0 = 2L_{\text{EQ}}/c$ is generally set to $\tau_0 = 533 \ \mu s$ ($L_{\text{EQ}} = 80$ km) [23], [24]. The numerical solution of (15) is shown in Fig. 2 (top) for the case of MARSIS ($f_A = 3$ MHz and $f_B = 4$ MHz) and for different L_{eq} values.

The UWB processing provides that time-delay offset recovery is performed via echo retracking. In our work, we found that the offset center of gravity (OCOG) [25] is the one that provides the best results for our purposes among the tested algorithms and is thus selected to be implemented in the processing.

Time offset estimation between the two subbands can be challenging due to topographic effects that produce errors in the surface tracking. Such errors are due to the decorrelation of the speckle of echoes acquired at different frequencies. These effects have been mitigated by processing MARSIS data using a delay Doppler algorithm [26], which is based on the incoherent summation of the superimposed filters acquired at different synthetic apertures.

B. Ionospheric Attenuation Compensation

The two-way total attenuation [29] caused by the ionosphere can be expressed in the frequency domain as

$$\alpha(f)|_{\text{dB}} = 9.2 \times 10^4 \int_0^{h_{\text{max}}} \left(\frac{f_p(Z)}{8.98}\right)^2 \frac{\nu(z)}{(2\pi f)^2 + \nu^2(z)} dz \qquad (16)$$
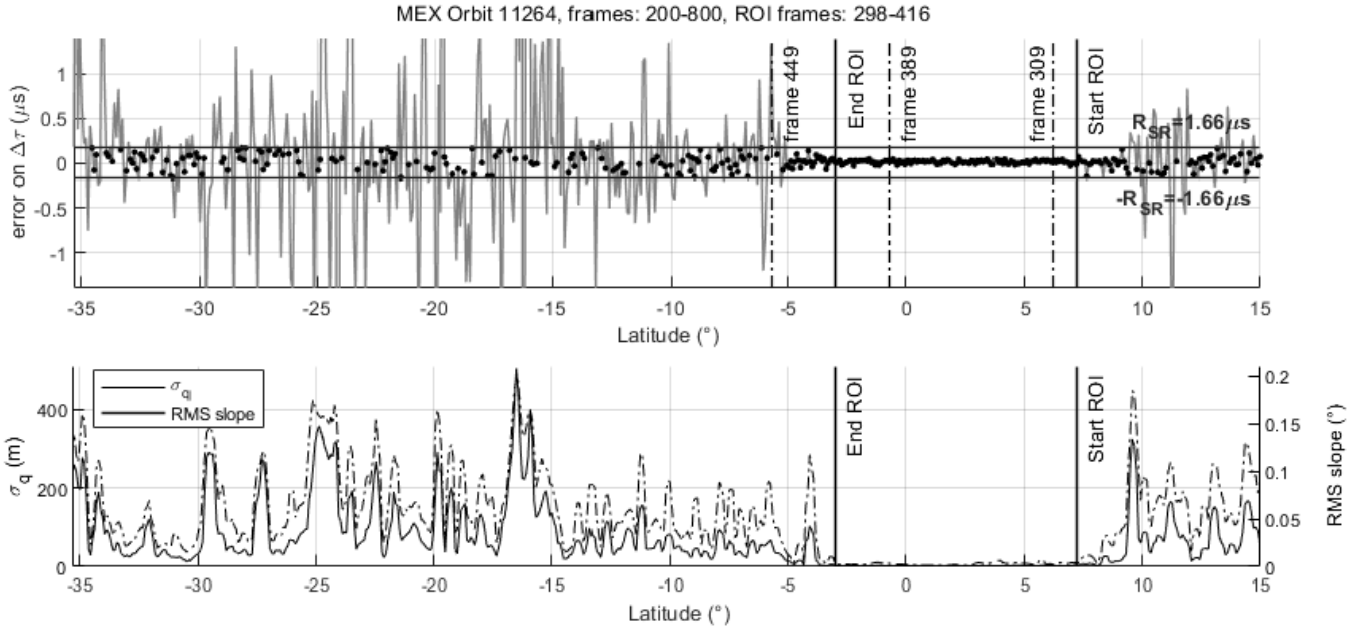
Fig. 7. (Top) $\Delta\tau$ error estimation from the ID 11264 ray-traced MOLA simulation acquired on channels B2 and B3. Black dots highlight the frames where the processing is expected to be successful as the $\Delta\tau$ error between the echoes lies between the limit obtained in Section IV ($\pm R_{SR}$ in black horizontal lines). The flat section in between the vertical lines (which we refer to as end and start ROI, from $-3°$ to $8°$ of latitude) corresponds to the green orbit section highlighted in Fig. 6. (Bottom) Roughness metrics, σ_q and rms slope, calculated from the same track. These metrics are computed frame-by-frame over MARSIS footprint. The comparison between the two plots shows that in the case of a low-roughness regime area, the $\Delta\tau$ error is expected to guarantee the successful application of the processing.

that depends on the plasma frequency profile $f_p(z)$ and the electron's collision frequency ν.

To compute $\alpha(f)$, we exploit the Gamma parametric model, which describes the distribution of plasma frequency as a function of the ionosphere height [26]

$$f_p(z) = f_{p,\max} \frac{z - h_0}{b} e^{1 - \frac{z - h_0}{b}} \delta_{-1}(z - h_0) \qquad (17)$$

where $f_{p,\max}$ is the maximum plasma frequency referred to the ionosphere vertical profile, h_0 is the topside ionosphere layer height, and b is the shape factor. Based on [28], we set the altitude of the ionosphere at $h_0 = 120$ km reducing the model to two parameters: the maximum plasma frequency $f_{p,\max}$ and the shape factor b. The resulting dispersive attenuation is shown in Fig. 3 for different $f_{p,\max}$ values [28], [29]. As $f_{p,\max}$ and b are unknown quantities, we expressed the model as a function of $f_{p,\text{eq}}$ and L_{eq} by means of the following relationships [30]:

$$f_{p,\max} = 1.2 f_{p,\text{eq}} \qquad (18)$$
$$b = 0.37 L_{\text{eq}} \qquad (19)$$

where $f_{p,\text{eq}}$ is obtained from (15).

The main steps for ionosphere attenuation correction exploited in the UWB processing are summarized as follows:

1) equivalent plasma frequency estimation from the time delay;
2) conversion of the SPEM into the Gamma model;
3) computation of the attenuation function through $f_{p,\max}$.

C. Phase Offset Estimation

Phase offset is generated by the propagation of the signal through ionosphere (represented by the constant term in the SPEM model). We pursue its estimation by the least-squared estimation (LSE) approach using the signal subbands. Both the complex components of the lower and higher spectra are forward and backward extrapolated to completely overlay. The selected phase offset correction is the one that minimizes the mse between the measured and the extrapolated samples.

V. RESULTS FROM SIMULATED DATA

Here, we apply the processing to MARSIS-simulated data. Specifically, we use a point-scatter simulator to both validate the sixfold improvement in resolution and evaluate the tolerable time-delay error for ensuring the correct application of the method. Instead, ray-traced MOLA simulations are employed for preselecting the areas that fulfill this condition.

A. Point-Scatter Simulator

For the purpose of verifying the resolution enhancement, the UWB technique is applied to the simulated response of two-point scatterers placed at the resolution limit. Specifically, Fig. 4 (right) shows the real part of the simulated full 6-MHz bandwidth (black dotted line) and the UWB processed spectrum (black solid line), obtained from the 1-MHz subbands at ± 0.5 MHz (gray line). After fast Fourier transform (FFT), we obtain the responses in Fig. 4 (left), where the two echoes, previously unresolved, can now be easily identified.

Another crucial aspect to constrain the applicability of the algorithm is the analysis of surface topographic effect.
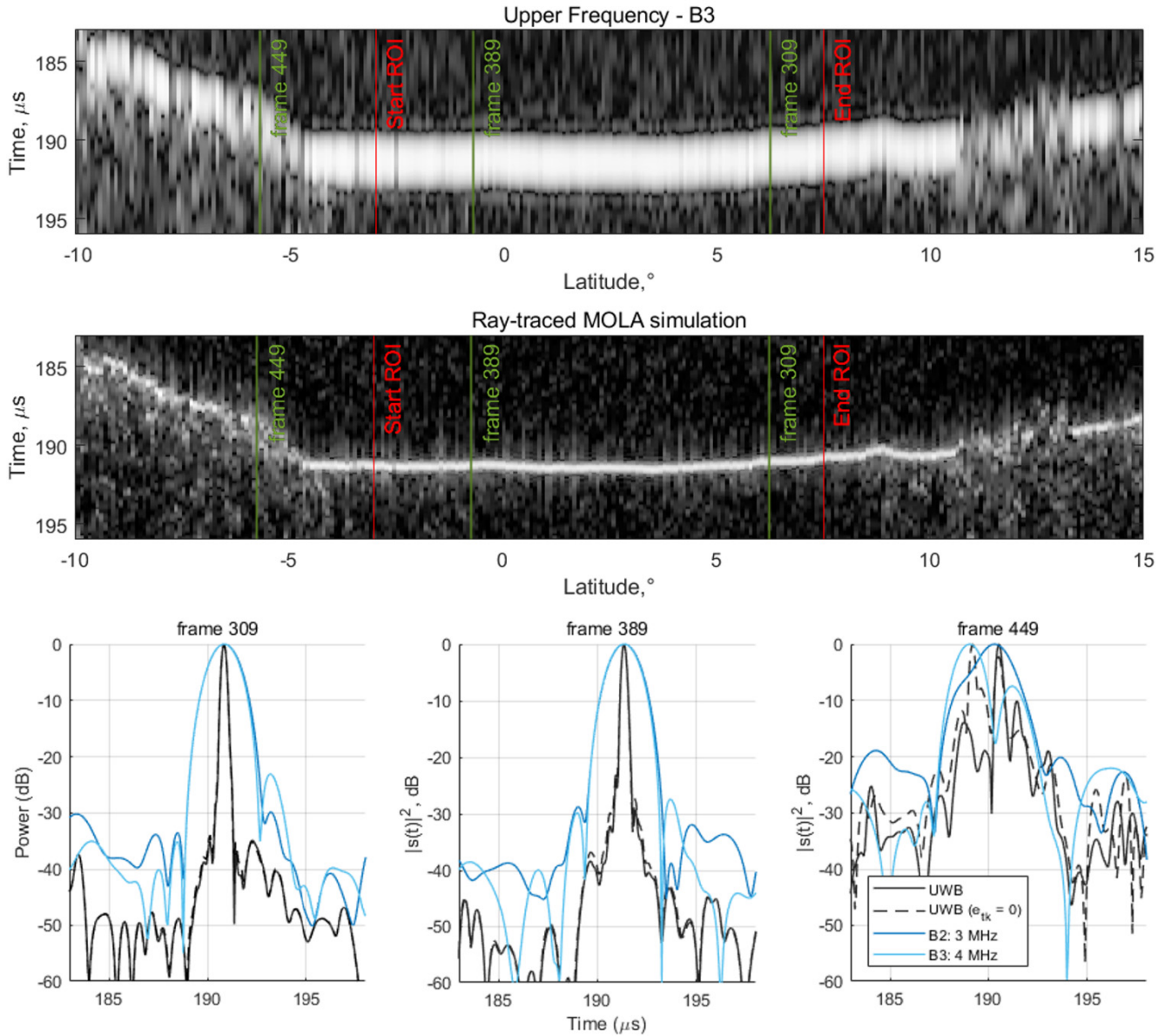
Fig. 8. Application of the UWB processing at the ray-traced MOLA simulated product ID 11264. (Top) Simulated product on band B3. (Bottom) Its UWB processed version. The red vertical lines specify the beginning and the end of the ROI (Elysium Planitia) where the processing is expected to be successful. Instead, the green lines refer to frames 309, 389, and 449. (Bottom) The frame-by-frame comparison is done considering two cases: $\Delta\tau$ retracker estimation and correction (black solid line) and no $\Delta\tau$ correction, representing the ideal case (black dot line). As selected within a flat regime area, frames 309 and 389 are characterized by the successful application of the processing: the two SR echoes are essentially indistinguishable. This is not verified by frame 409 that shows two different super-resolved echoes for the two $\Delta\tau$ corrections. In fact, in the case of $e_{tr} = 0$, we obtain a waveform with features we attribute to off-nadir clutter, while in another case, the processing results in the arising of spurious echoes due to the use of an inaccurate time correction to the two subbands.

These cause the tracker to make errors in the time-delay estimation when tracking the surface at different frequencies $e_{trk} = \Delta\tau_{real} - \Delta\tau_{trk}$.

In Fig. 5, we show the comparison between the simulated full 6-MHz bandwidth point-scatter response (dotted line) and the reconstructed signal after UWB (black solid line) at varying e_{trk} (multiple of R_{SR}, the expected theoretical range resolution after UWB processing) and after Hanning weighting.

In the case of perfect alignment, the simulated and the super-resolved echoes almost overlay. This condition is not verified

for increasing error values: the final products show signs of evident echo distortions such as the arising of spurious echoes and losses in resolution that becomes more relevant as the misalignment increases. For the case of MARSIS, we consider the value of -22 dB as a limit for the required signal dynamic after Hanning weighting [1] that corresponds to a maximum tolerable time-delay error equal to $e_{trk} = R_{SR}$. As MARSIS design range resolution is about $R_r = 1$ μs, $R_{SR} = R_r/6$ value is expected to be equal to 0.166 μs.

Note that the simulations presented in this section employ MARSIS design parameters. However, this analysis can be
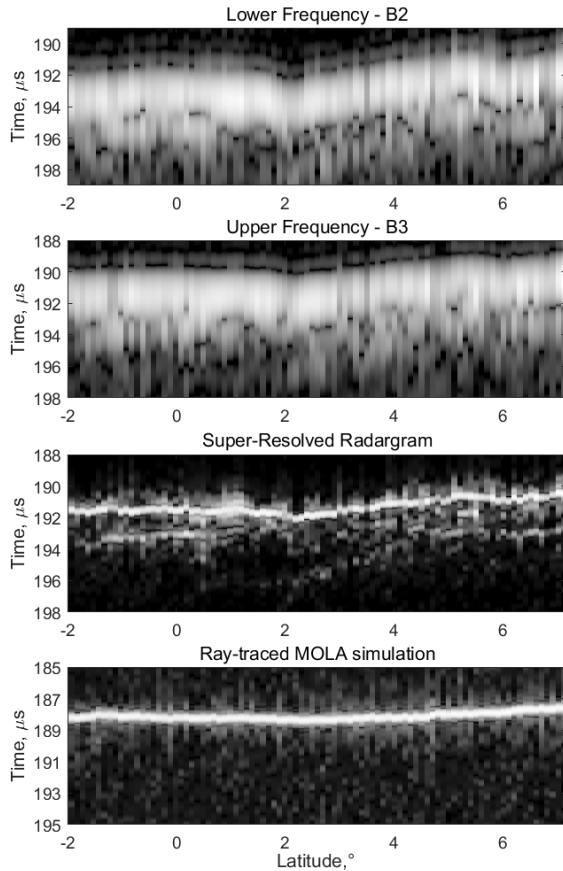
Fig. 9. Application of UWB processing to ID 11264 MARSIS experimental and ray-traced simulated products acquired over Elysium Planitia (green line in Fig. 5). The middle and bottom refer to the experimental and simulated UWB processed products, respectively. The enhancement in terms of range resolution highlights several features (at ∼0°N and ∼5°N) previously not clearly visible. As these features do not appear in the simulated radargram, we attribute them to shallow interfaces.

easily generalized and carried out on multifrequency radar systems with different characteristics.

B. Response From Facets Simulator

With the aim to derive the conditions for the applicability of the algorithm in relation to Mars topography, time-delay, and phase offset estimation is pursued on coherent simulated data on three Doppler filters. The simulator employs the facet method applied to MOLA data to determine Mars surface radar response as described in [15].

We applied the processing to the ray-traced MARSIS-simulated product ID 11264 (see Fig. 6 with a white-green line) consisting of acquisitions over several areas at different roughness regimes.

Fig. 7 (top) and (bottom) shows the along track e_{trk} obtained from the difference of the tracking algorithm applied to the same product at the two bands B2 and B3. In the top, the gray line indicates e_{trk} as a function of latitude, while the black dots highlight the frames where the applicability condition (represented by two horizontal black lines) of the algorithm is fulfilled. The bottom shows the root-mean-square (rms) height (σ_q) and the rms slope calculated along the ground track using MOLA MEGDRs data. The on-ground illuminated

area is computed using the along-track (considering the three Doppler filters) and cross-track resolution (the pulse-limited diameter). In particular, rms height is calculated after removing the 2-D mean slope through a linear regression model. The graphs show that the region characterized by low-roughness level (see latitudes between −3° and 8°) fulfills the criterion on e_{trk}. This area, identified as Elysium Planitia, is known for its flat topography and thus selected as region of interest (ROI) for testing our algorithm. We found that σ_q is less than $\lambda/16$ when compared to the wavelength of MARSIS, meaning a low regime roughness and thus a dominant presence of coherent scattering.

With the aim to evaluate the time offset errors, a statistical analysis is performed over three areas of different roughness regimes (see Fig. 5).

Region 1: Smooth area between −2° and 8°N and 164° and 170°E (3763 frames and 36 orbits).

Region 2: Moderate rough area between −3° and −13°N and 164° and −170°E (3319 frames and 35 orbits).

Region 3: Rough region between −17° and −30°N and 128° and −138°E (8110 frames and 64 orbits).

We selected all the currently available acquisitions (at B2 and B3 bands) and found that most of the echoes acquired in region 1 satisfy the condition on of e_{trk} (nearly 99%). As expected, e_{trk} increases for regions 2 and 3 causing a lower success percentage of the algorithm in fulfilling the above-mentioned limit. This consideration confirms that the UWB processing can be successfully applied on smooth surfaces where the constraint on time offset is satisfied, thus yielding more accurate results.

Fig. 8 shows the ray-traced MOLA simulation ID 11264 and, from left to right, a comparison between the frames 309 and 389 acquired within the ROI and frame 449 from a rougher region before (dark and light blue lines for B2 and B3, respectively). The picture displays both the original (top) and the processed product (middle).

Since simulations do not include ionospheric distortion, we evaluated the tracking errors on data with no time offset. Two cases are considered: no time offset realignment, corresponding to the case of $e_{trk} = 0$, thus yielding the ideal super-resolved waveform (black dotted line) and after $\Delta\tau$ retracking process (black solid line).

Note that the retracking algorithm does not introduce significant errors when considering echoes acquired over a flat region as the resulting responses overlay. On the other hand, the results from frame 449 show clear differences between the two waveforms, pointing out the failure of the processing. In particular, the ideal super-resolved product is characterized by what we consider unresolved off-nadir clutter.

VI. RESULTS FROM EXPERIMENTAL MARSIS DATA

We applied the algorithm to data acquired over different areas of Mars, each characterized by a low-roughness regime, thus fulfilling the time-delay realignment condition. Selected products are acquired under nighttime conditions (solar zenith angle (SZA) > 90°), as ionosphere effects do not degrade the full-band estimation on relatively smooth
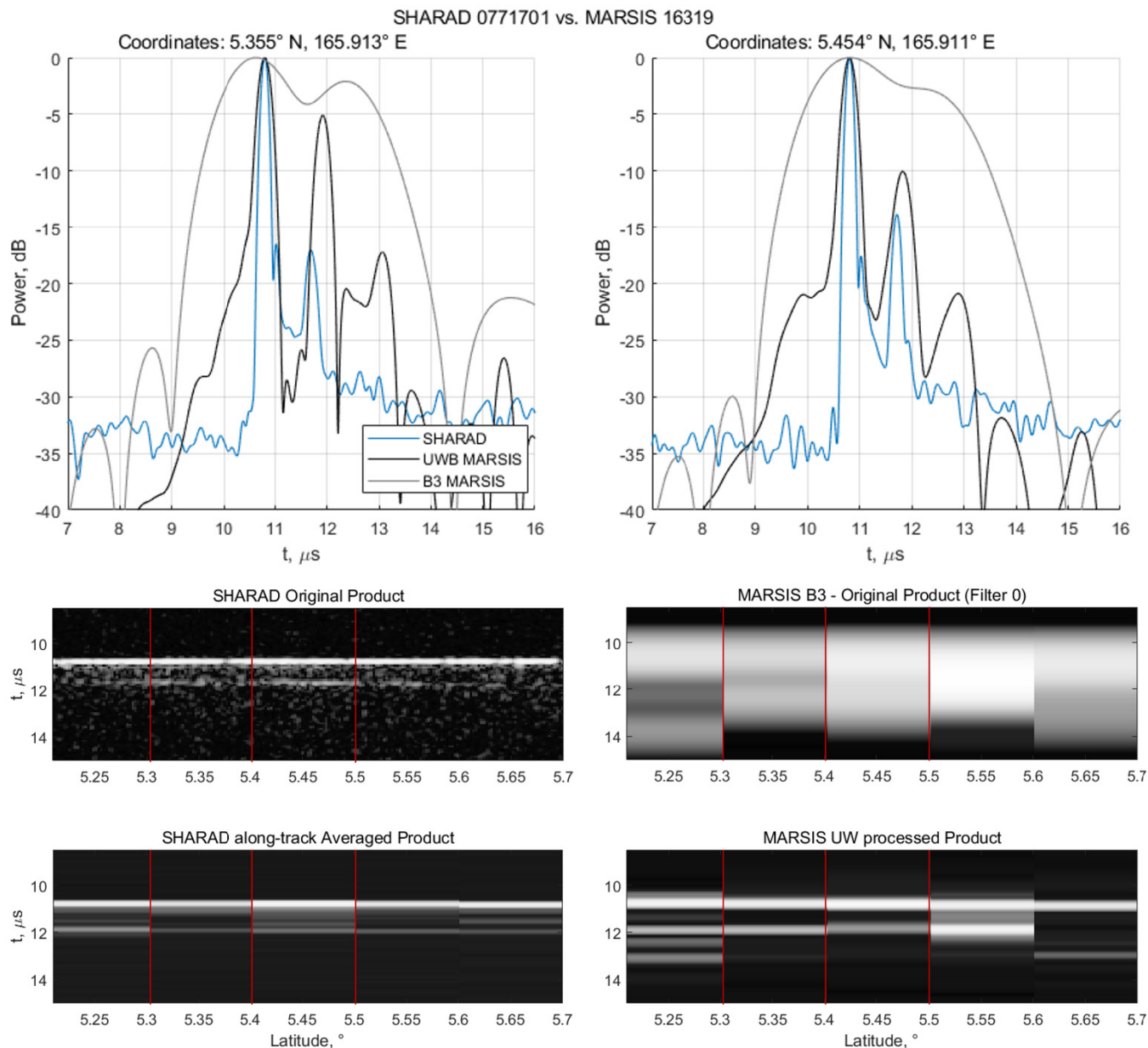
Fig. 10. Comparison between SHARAD product ID 07701701 and MARSIS product ID 16319 acquired over Elysium Planitia (acquired at the crossover in Fig. 6). Ground tracks are shown in red and in green solid lines in Fig. 6. (Top) Frame-by-frame comparison between the MARSIS (gray line) and SHARAD (blue line) standard products and the UWB MARSIS product (black line). (Middle) SHARAD and MARSIS standard products. The lower MARSIS resolution (150 m in free space) does not allow the detection of the subsurface layer, which appears unresolved if compared to the SHARAD product. (Bottom) Averaged version of the SHARAD data product in order to maintain the same along-track resolution of MARSIS is compared with the UWB MARSIS product. Note that the same shallow interface detected from SHARAD data now arises in the UWB processed product.

surfaces, unless in the case of low SNR, when a fine retracking procedure is not achievable.

We present the results from the equatorial region Elysium Planitia and from three different areas at the south polar layered deposits (SPLD): Planum Australe, Promethei Lingula, and the so-called radar unit reflection-free zones (RFZs).

A. Elysium Planitia

Elysium Planitia is a multilayer volcanic plain, characterized by basaltic flow complex stratigraphy, whose layers' thicknesses range from 16 to 50 m [31]. The entire area in the past

years has been targeted with the aim of searching for buried ice resources.

The top in Fig. 9 shows the original B3 radargrams, while the middle and bottom ones show the super-resolved experimental and simulated products, respectively. As we can see, there is evident mismatch between both the surface topography obtained from experimental radargrams and simulated data. We attribute such mismatch to the time delay introduced by the ionosphere. As a consequence, this effect is also present on the super-resolved product where the surface follows B3 product topography as the UWB
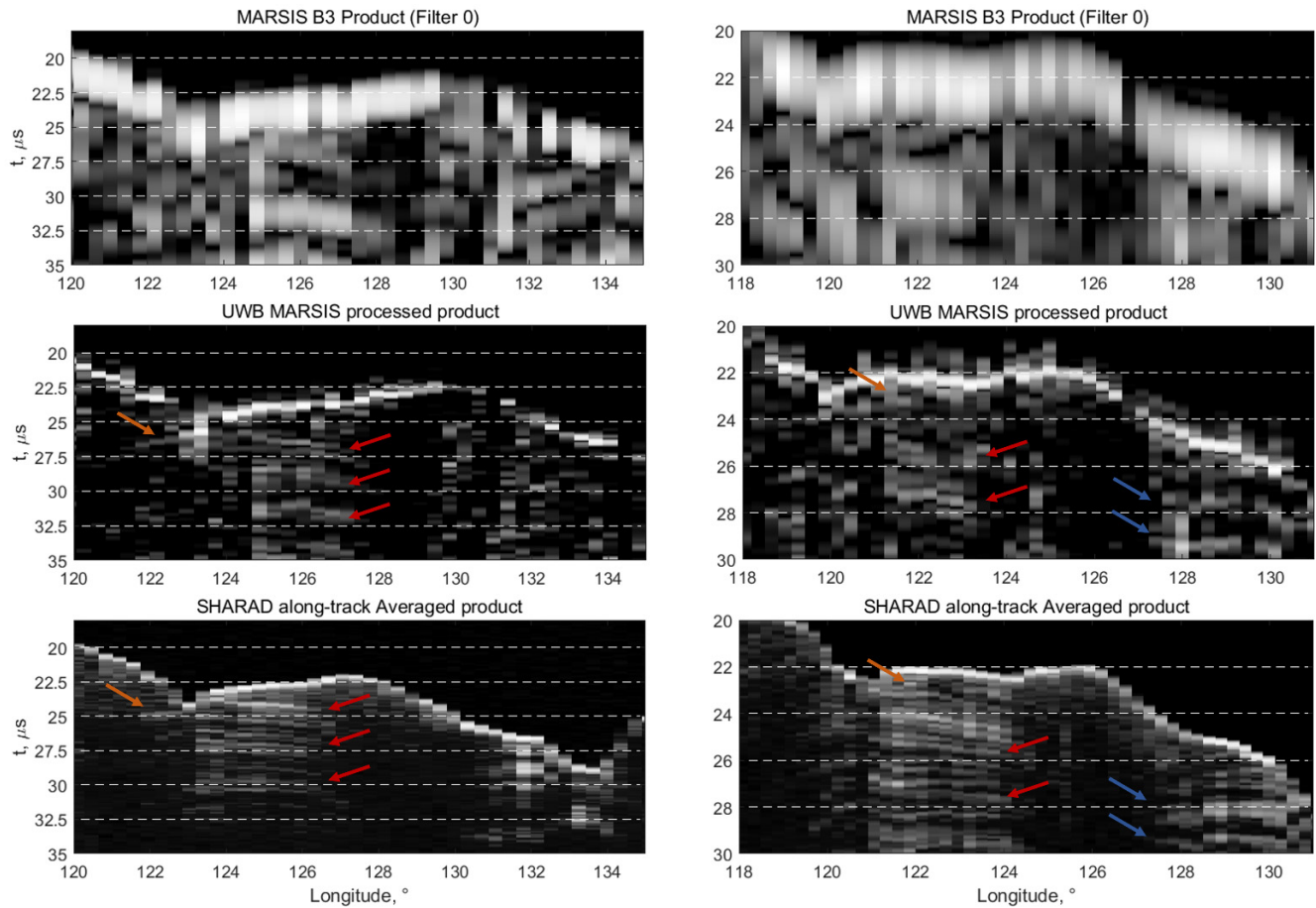
Fig. 11. Comparison (left) between MARSIS product ID 10646 and SHARAD product ID 3320701 and (right) between MARSIS product ID 2978 and SHARAD product ID 537120 acquired over Promethei Lingula. The top and middle refer to the B3 MARSIS original and the UWB processed product, respectively, while the bottom refers to the SHARAD along-track averaged product. The four graphs in the bottom represent a frame-by-frame comparison between the three abovementioned data. We observe the detection of two packets of reflectors, at nearly 121°–126°E (red arrows) and 128°–130° (blue arrows). These structures are detected even by SHARAD. Moreover, a feature previously under standard resolution (orange arrow) is now visible from the data.

processing provides for the time alignment of the B2 over the B3 echoes.

After processing, MARSIS super-resolved product shows the presence of a secondary signature previously not evident in the original product due to the limited range resolution. From inspection of the super-resolved simulated product, we identified these reflections, as subsurface shallow structures located at latitudes around 0°, 5.5°, and 7°N.

To further validate our results, we selected several MRO and MEX orbital crossovers acquired over the same ROI and compared super-resolved MARSIS products with original SHARAD ones.

In Fig. 10, we plot a MARSIS waveform (product ID 16319) after UWB, with SHARAD (product ID 07701701) echoes collected at the same location on Mars (around 5.5°N–166°E), as shown in Fig. 5. To have a direct comparison between data acquired by the two sounders, we averaged several frames of the SHARAD radargram to obtain a similar along-track resolution compared to MARSIS products. Now, after UWB processing, the subsurface returns observed in SHARAD are also clearly visible in the UWB MARSIS product. Furthermore, the processed radargrams show a more accurate estimation of

the shallow reflector depth, previously appearing right shifted due to the weak resolution, and now almost aligned with the subsurface SHARAD echo.

B. South Polar Layered Deposits

SPLDs are the largest reservoir of water ice on Mars. They are predominantly composed by dusty ice with a perennial cap of CO_2 ice and on top of it a thin layer of seasonal CO_2 frost that condensates and sublimates during every Martian year. Under the residual cap, a massive deposit of buried CO_2 ice also called "reflection-free zone three" (RFZ3) has been mapped in detail by SHARAD [32]. Hundreds of kilometers southward, a plain called Planum Australe has been probed by MARSIS several times frequently showing strong reflections from subsurface structures [33].

Here, we present the application of UWB processing over three different regions that characterize the SPLD.

Fig. 11 (left) and (right) shows two different products acquired over Promethei Lingula (124°E–82.5°S) before and after UWB processing (top and middle). As we can see, the processing enables to detect the same subsurface stratigraphy outlined by the data from SHARAD orbital
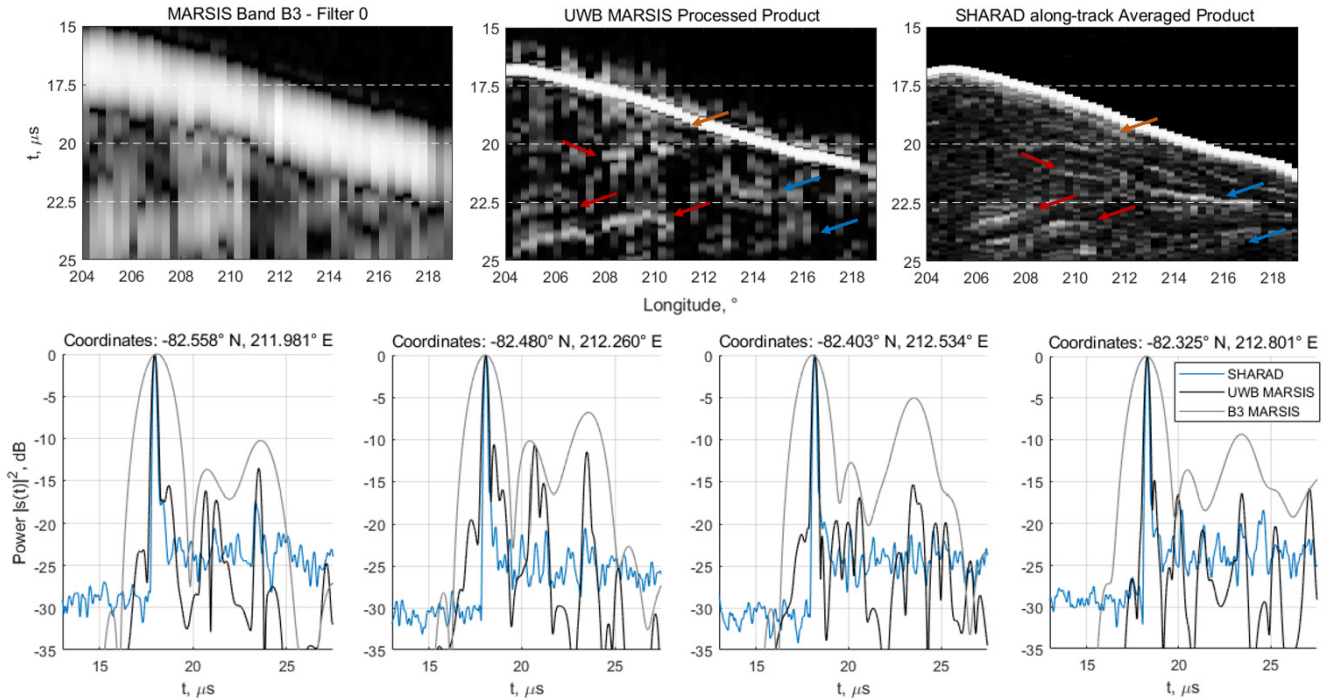
Fig. 12. Comparison between SHARAD product ID 2719101 and MARSIS product ID 1287 acquired over the central portion of Planum Australe. (Top-Left) B3 MARSIS original product. (Top-Center) Relative UWB processed version. (Top-Right) SHARAD along-track averaged product. (Bottom) Frame-by-frame comparison between the three abovementioned data. Through the comparison of the UWB processed product and SHARAD, it is possible to notice the detection of many interfaces previously not observable from the MARSIS original data: (a) very shallow reflector at the limits of the UWB resolution (at about 211°E), (b) interface on the left side of the radargram (∼ 3 μs depth), and (c) detection of two deep subsurface layers at the right side previously merged in one reflector in the original product (∼5.5 μs depth). Note that how the UWB MARSIS data product appears less attenuated if compared to SHARAD data due to the difference between the two operative frequencies.
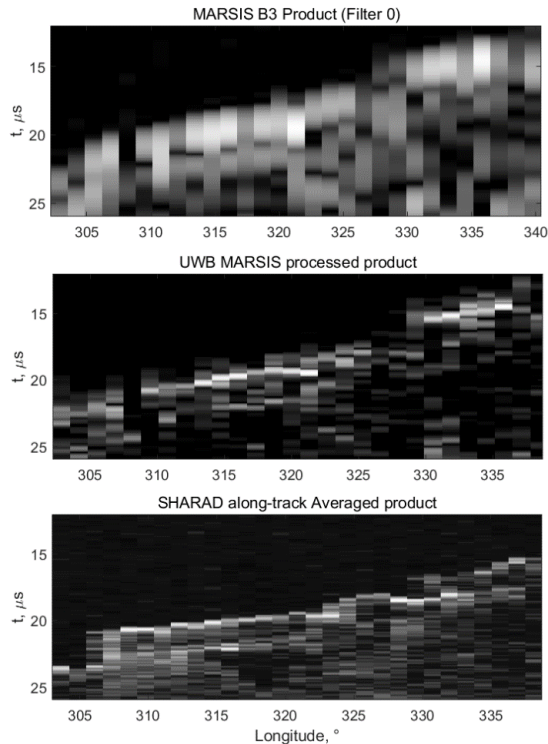

Fig. 13. (Top) Standard MARSIS data product (ID 12875) acquired over the RFZ3. (Middle) MARSIS product after UWB processing, note that the enhancement in resolution enables the detection of one of the three CO_2 sub-units capped by water ice. (Bottom) SHARAD product ID 3629501 acquired over the same area. The two products have a comparable resolution (25 versus 15 m) and are able to detect the same layer at about 22.5 μs.

crossover (bottom). Specifically, the UWB products highlight two packets of reflectors, at about 121°–126°E (red arrays) and at 129°–130° (blue arrays). Sometimes, many features visible in SHARAD radargrams cannot be found in the MARSIS product and vice versa. We believe that this could be due to some possible differences in acquisition geometries or due to subsurface structures, which appear different when observed at different wavelengths [34], [35].

In Fig. 12, we show the results from the central area of Planum Australe (220°E–82.5°S). Here, the processing enables the detection of three new features: a very shallow reflector at the limits of UWB resolution (at about 211°E, orange arrow), two subsurface layers located around 5.5 μs depth previously merged in a single reflector (red arrows), and a shallow layer at 3 μs depth (blue arrows). These subsurface structures recurrently appear in MARSIS super-resolved products over this area and, furthermore, can be easily matched with the interfaces visible from SHARAD radargrams.

Finally, Fig. 13 shows a product acquired over the CO_2 deposits, located (at around 86.7°–87.2°S). This region with reflection-free subsurface zone has been proven to be composed of sequestered low-porosity carbon dioxide ice [33]. Its boundaries, not clearly visible from the original MARSIS data, can now be resolved due to UWB processing.

VII. CONCLUSION

In this article, we apply the UWB processing to experimental MARSIS data reaching an improvement in range resolution up to 25 m. The method, based on AR models,

is applicable to multifrequency sounders and provides for the fusion of the two quasi-simultaneously acquired data via BWI and BWE to further increase signal bandwidth. To deal with the MARSIS case, we had to address the ionospheric effects by compensating time delay, amplitude distortions, and phase offset of the signals received at the two channels via retracking, ionospheric modeling, and spectral prediction.

Using point-scatter and ray-traced MOLA sounder simulations, we investigated the applicability of the method and constrained the maximum tracking error due to topography, which allows to apply the algorithm without incurring in evident signal distortions or formation of paired echoes.

Finally, we applied the technique to experimental data acquired over selected low-regime roughness regions of Mars. The processing provides enhanced imaging performances on different scenarios: several interfaces that are not visible in the original MARSIS data can be clearly detected after UWB processing and confirmed by SHARAD products.

Future works aim to obtain a more accurate estimation of Mars surface and subsurface dielectric properties via the joint application of data inversion methodologies using UWB processed MARSIS and SHARAD data. An improvement in accuracy in the loss tangent could be achievable due to the lower medium attenuation that affects MARSIS data as acquired on a lower frequency with respect to SHARAD [35], [36].

The technique here proposed has general applicability and could be helpful for the interpretation of radar data acquired by future planetary missions, for example, in the case of a multifrequency radar system for the exploration of icy moons [37] or in the context of water ice research on Mars [38].
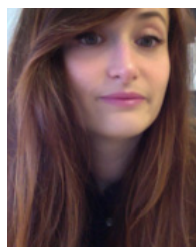
ACKNOWLEDGMENT

REFERENCES

[1] R. Jordan et al., "The Mars express MARSIS sounder instrument," *Planet. Space Sci.*, vol. 57, nos. 14–15, pp. 1975–1986, Sep. 2009.

[2] R. Seu et al., "SHARAD sounding radar on the Mars reconnaissance orbiter," *J. Geophys. Res.*, vol. 112, May 2007, Art. no. E05S05.

[3] G. Picardi et al., "MARSIS: Mars advanced radar for subsurface and ionosphere sounding," in *Mars Express: The Scientific Payload*. 2004, pp. 51–69. [Online]. Available: https://ui.adsabs.harvard.edu/abs/2004ESASP1240...51P/abstract

[4] G. Picardi, S. Sorge, R. Seu, G. Fedele, C. Federico, and R. Orosei, "Mars advanced radar for subsurface and ionosphere sounding (MARSIS): Models and system analysis," INFOCOM, Rome, Italy, Tech. Rep. N.MRS-001/005/99, Mar. 1999.

[5] K. M. Cuomo, "A bandwidth extrapolation technique for improved range resolution of coherent radar data," MIT Lincoln Lab., Lexington, MA, USA, Project Rep. CJP60, Revision, Tech. Rep., Dec. 1992, vol. 1. [Online]. Available: https://apps.dtic.mil/sti/pdfs/ADA258462.pdf

[6] T. G. Moore, B. W. Zuerndorfer, and E. C. Burt, "Enhanced imagery using spectral-estimation-based techniques," *Lincoln Lab. J.*, vol. 10, no. 2, pp. 171–186, 1997.

[7] K. M. Cuomo, J. E. Pion, and J. T. Mayhan, "Ultrawide-band coherent processing," *IEEE Trans. Antennas Propag.*, vol. 47, no. 6, pp. 1094–1107, Jun. 1999.

[8] M. C. Raguso, M. Mastrogiuseppe, R. Seu, and L. Piazzo, "Super resolution and interferences suppression technique applied to SHARAD data," in *Proc. 5th IEEE Int. Workshop Metrology Aerosp. (MetroAeroSpace)*, Jun. 2018, pp. 242–246, doi: 10.1109/MetroAeroSpace.2018.8453529.

[9] M. C. Raguso, L. Piazzo, M. Mastrogiuseppe, R. Seu, and R. Orosei, "Resolution enhancement and interference suppression for planetary radar sounders," in *Proc. 26th Eur. Signal Process. Conf. (EUSIPCO)*, Rome, Italy, Sep. 2018, pp. 1222–1226.

[10] M. Mastrogiuseppe et al., "The bathymetry of a Titan Sea," *Geophys. Res. Lett.*, vol. 41, no. 5, pp. 1432–1437, Mar. 2014, doi: 10.1002/2013GL058618.

[11] V. Poggiali et al., "The bathymetry of moray sinus at Titan's Kraken Mare," *J. Geophys. Res. Planets*, vol. 125, no. 12, Dec. 2020, Art. no. e2020JE006558.

[12] N. Oudart et al., "Range resolution enhancement of WISDOM/ExoMars radar soundings by the bandwidth extrapolation technique: Validation and application to field campaign measurements," *Planet. Space Sci.*, vol. 197, Mar. 2021, Art. no. 105173, doi: 10.1016/j.pss.2021.105173.

[13] D. E. Smith et al., "Mars orbiter laser altimeter: Experiment summary after the first year of global mapping of Mars," *J. Geophys. Res. Planets*, vol. 106, no. E10, pp. 23689–23722, Oct. 2001.

[14] G. Picardi et al., "Radar soundings of the subsurface of Mars," *Science*, vol. 310, no. 5756, pp. 1925–1928, 2005, doi: 10.1126/science.1122165.

[15] J.-F. Nouvel, A. Herique, W. Kofman, and A. Safaeinili, "Radar signal simulation: Surface modeling with the facet method," *Radio Sci.*, vol. 39, no. 1, Feb. 2004, Art. no. RS1013, doi: 10.1029/2003RS002903.

[16] G. Picardi et al., "The subsurface investigation by Mars Advanced Radar for subsurface and ionosphere sounding (MARSIS)," in *Proc. Int. Geosci. Remote Sens. Symp. Taking Pulse Planet, Role Remote Sens. Manag. Environ. (IGARSS)*, Jul. 2000, pp. 1730–1732, doi: 10.1109/IGARSS.2000.857863.

[17] G. Alberti et al., "SHARAD radar signal processing technique," in *Proc. 4th Int. Workshop Adv. Ground Penetrating Radar*, Jun. 2007, pp. 261–264.

[18] S. B. Bowling, "Linear prediction and maximum entropy spectral analysis for radar applications," MIT Lincoln Lab., Lexington, MA, USA, Project Rep. RMP-122, Revision, Tech. Rep., May 1977, vol. 4. [Online]. Available: https://apps.dtic.mil/sti/pdfs/ADA042817.pdf

[19] J. E. Piou, K. M. Cuomo, and J. T. Mayhan, "A state-space technique for ultrawide-bandwidth coherent processing," MIT Lincoln Lab., Lexington, MA, USA, Project Rep., Tech. Rep., Jul. 1999, vol. 1054. [Online]. Available: https://apps.dtic.mil/sti/pdfs/ADA366105.pdf

[20] D. J. Daniels, *Ground Penetrating Radar*. Stevenage, U.K.: Institution of Electrical Engineers, 2004.

[21] S. M. Kay, "Autoregressive spectral estimation: Methods," in *Modern Spectral Estimation: Theory and Application*. Englewood Cliffs, NJ, USA, Prentice-Hall, 1988.

[22] M. C. Raguso, "Sounder data processing and techniques for geophysical parameters estimation," Ph.D. dissertation, Dipartimento di Ingegneria dell'Informazione, Elettronica e Telecomunicazioni, DIET, La Sapienza, Roma, RM, Italy, 2018.

[23] D. Biccari, G. Picardi, and R. Seu, "Adaptive compensation of Mars ionosphere dispersion in the MARSIS experiment," in *Proc. IEEE Int. Geosci. Remote Sens. Symp. (IGARSS)*, Jul. 2001, pp. 2557–2559, doi: 10.1109/IGARSS.2001.978087.

[24] G. Picardi and S. Sorge, "Adaptive compensation of ionosphere dispersion to improve subsurface detection capabilities in low-frequency radar systems," in *Proc. 8th Int. Conf. Ground Penetrating Radar*, Apr. 2000, pp. 624–629, doi: 10.1117/12.383540.

[25] D. J. Wingham, C. G. Rapley, and H. Griffiths, "New techniques in satellite altimeter tracking system," in *Proc. IGARSS*, Zurich, Switzerland, Sep. 1986, pp. 1–6.

[26] V. Poggiali et al., "High-resolution topography of Titan adapting the delay/Doppler algorithm to the Cassini RADAR altimeter data," *IEEE Trans. Geosci. Remote Sens.*, vol. 57, no. 9, pp. 7262–7268, Apr. 2019, doi: 10.1109/TGRS.2019.2912575.

[27] A. Safaeinili, W. Kofman, J. F. Nouvel, A. Herique, and R. L. Jordan, "Impact of Mars ionosphere on orbital radar sounder operation and data processing," *Planetary Space Sci.*, vol. 51, pp. 505–515, Mar. 2003.

[28] P. Withers, "Attenuation of radio signals by the ionosphere of Mars: Theoretical development and application to MARSIS observations," *Radio Sci.*, vol. 46, no. 2, pp. 1–16, Apr. 2011, doi: 10.1029/2010RS004450.

[29] A. Safaeinili et al., "Radar sounding of Mars: A focus on MARSIS," in *Proc. Conf. Geophys. Detection Subsurface Water Mars*, Aug. 2001, pp. 92–93.

[30] G. Picardi et al., "Mars ionosphere data inversion by MARSIS surface and subsurface signals analysis," in *Proc. IEEE Radar Conf.*, May 2008, pp. 1–5, doi: 10.1109/RADAR.2008.4720760.

[31] G. Morgan et al., "Evidence for the episodic erosion of the Medusae Fossae Formation preserved within the youngest volcanic province on Mars," *Geophys Res. Lett.*, vol. 42, no. 18, pp. 7336–7342, 2015.

[32] R. J. Phillips et al., "Massive CO_2 ice deposits sequestered in the south polar layered deposits of Mars," *Science*, vol. 332, no. 6031, pp. 838–841, 2011.

[33] R. Seu et al., "Accumulation and erosion of Mars' south polar layered deposits," *Science*, vol. 317, no. 5845, pp. 1715–1718, 2007.

[34] B. A. Campbell, G. A. Morgan, F. Bernardini, N. E. Putzig, D. C. Nunes, and J. J. Plaut, "Calibration of Mars reconnaissance orbiter shallow radar (SHARAD) data for subsurface probing and surface reflectivity studies," *Icarus*, vol. 360, May 2021, Art. no. 114358, doi: 10.1016/j.icarus.2021.114358.

[35] B. A. Campbell and G. A. Morgan, "Fine scale layering of Mars polar deposits and signatures of ice content in nonpolar material from multiband SHARAD data processing," *Geophys. Res. Lett.*, vol. 45, no. 4, pp. 1759–1766, Jan. 2017, doi: 10.1002/2017GL075844.

[36] G. Picardi et al., "MARSIS data inversion approach: Preliminary results," in *Proc. IEEE Radar Conf.*, May 2008, pp. 1–4.

[37] M. Mastrogiuseppe, "Dual frequency orbiter-radar system for the observation of seas and tides on titan: Extraterrestrial oceanography from satellite," *Remote Sens.*, vol. 11, no. 16, p. 1898, Aug. 2019.

[38] G. Morgan et al., "Availability of subsurface water-ice resources in the northern mid-latitudes of Mars," *Nature Astron.*, vol. 5, pp. 230–236, Mar. 2021.

M. C. Raguso received the M.Sc. degree in communication engineering and the Ph.D. degree in radar systems and remote sensing from the University of Rome Sapienza, Rome, Italy, in 2015 and 2018, respectively.

From 2015 to 2017, she was Visiting Ph.D. Student with the Cornell Center for Astrophysical Science, Cornell University, Ithaca, NY, USA. In 2018, she joined the Geology and Planetary Science Division, California Institute of Technology (Caltech), Pasadena, CA, USA, as a Post-Doctoral Researcher, working on Cassini SAR data. She is currently a NASA Post-Doctoral Fellow at the Jet Propulsion Laboratory (JPL), Caltech. Her research interests include radar system data processing, electromagnetic propagation, scattering theory, synthetic aperture radar (SAR), and the analysis of planetary radar sounder signals Mars Advanced Radar for Subsurface and Ionosphere Sounding (MARSIS) and Shallow Radar (SHARAD) for geophysical parameter estimation.
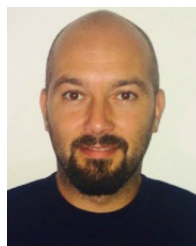
M. Mastrogiuseppe received the B.S., M.S., and Ph.D. degrees in telecommunication engineering from the Sapienza University of Rome, Rome, Italy, in 2005, 2008, and 2012, respectively.

From 2014 to 2016, he was a Research Associate with the Cornell Center for Astrophysical Science, Cornell University, Ithaca, NY, USA. He is currently a Researcher with the Dipartimento Elettronica e Telecomunicazioni (DIET), Sapienza University of Rome. He is a Team Member of the Shallow Radar (SHARAD) experiment on board of MRO and the Co-Lead of the Visar Instrument onboard of the VERITAS mission for the exploration of Venus. He was nominated as an Associate Team Member of the Cassini RADAR Science Team. He is the author of several articles. His research interests include remote sensing, radar system, data processing, and sounder data analysis for planetary exploration.

L. Gambacorta was born in Latina, Italy, in 1994. She received the B.S. degree in aerospace engineering and the Master of Science degree in space and astronautical engineering from the Università degli Studi La Sapienza di Roma, Rome, Italy, in 2017 and 2020, respectively, where she is currently pursuing the Ph.D. degree in radar and remote sensing with the Department of Information, Electronic and Telecommunications (DIET).

Her research interests include the analysis of planetary radar sounder signals [Mars Advanced Radar for Subsurface and Ionosphere Sounding (MARSIS) and Shallow Radar (SHARAD)] for information extraction purposes and the study of several data processing techniques oriented to improve sounding capabilities and enhance the quality of the sounder radar data products.

R. Seu was born in Carbonia, Italy, in February 1959. He received the master's degree in electronics engineering and the Ph.D. degree from the Università degli Studi La Sapienza di Roma, Rome, Italy, in March 1985 and in October 1990, respectively.

From 1992 to 2020, he was an Assistant Professor. He is currently an Associate Professor with the Università degli studi La Sapienza di Roma. He is also a Lecturer of the course of "Radar systems for space applications" and "Systems for air traffic control." During his Ph.D. degree, he has been always working on radar systems and mainly on radars for planetary observations. Since 1993, he has been a member of the Cassini Radar Science Team and the co-investigator of the experiment.